

## Georadar-derived estimates of firn density in the percolation zone, western Greenland ice sheet

Joel Brown,<sup>1,2</sup> John Bradford,<sup>1</sup> Joel Harper,<sup>2</sup> W. Tad Pfeffer,<sup>3</sup> Neil Humphrey,<sup>4</sup> and Ellen Mosley-Thompson<sup>5</sup>

Received 12 May 2011; revised 8 November 2011; accepted 11 November 2011; published 25 January 2012.

[1] Greater understanding of variations in firn densification is needed to distinguish between dynamic and melt-driven elevation changes on the Greenland ice sheet. This is especially true in Greenland's percolation zone, where firn density profiles are poorly documented because few ice cores are extracted in regions with surface melt. We used georadar to investigate firn density variations with depth along a  $\sim 70$  km transect through a portion of the accumulation area in western Greenland that partially melts. We estimated electromagnetic wave velocity by inverting reflection traveltimes picked from common midpoint gathers. We followed a procedure designed to find the simplest velocity versus depth model that describes the data within estimated uncertainty. On the basis of the velocities, we estimated 13 depth-density profiles of the upper 80 m using a petrophysical model based on the complex refractive index method equation. At the highest elevation site, our density profile is consistent with nearby core data acquired in the same year. Our profiles at the six highest elevation sites match an empirically based densification model for dry firn, indicating relatively minor amounts of water infiltration and densification by melt and refreeze in this higher region of the percolation zone. At the four lowest elevation sites our profiles reach ice densities at substantially shallower depths, implying considerable meltwater infiltration and ice layer development in this lower region of the percolation zone. The separation between these two regions is 8 km and spans 60 m of elevation, which suggests that the balance between dry-firn and melt-induced densification processes is sensitive to minor changes in melt.

**Citation:** Brown, J., J. Bradford, J. Harper, W. T. Pfeffer, N. Humphrey, and E. Mosley-Thompson (2012), Georadar-derived estimates of firn density in the percolation zone, western Greenland ice sheet, *J. Geophys. Res.*, 117, F01011, doi:10.1029/2011JF002089.

### 1. Introduction

[2] Temporal variations in firn density can partially explain observed changes in ice sheet surface elevation [Holland *et al.*, 2011] and can substantially influence mass balance calculations based on surface elevation observations [Zwally *et al.*, 2005; Helsen *et al.*, 2008]. Firn densification rates are related to mean annual air temperature [e.g., Herron and Langway, 1980], which varies both temporally and spatially over the Greenland ice sheet (GrIS). Thus, a solid

understanding of spatial variations in current firn density with depth profiles on the GrIS can help elucidate changes in firn density under a changing climate. Process-based firn densification models have increased our understanding of compaction rates in areas with little or no surface melt [e.g., Zwally and Li, 2002], but current observational constraints on firn density with depth are very poor in regions of the accumulation area receiving more than negligible amounts of melt.

[3] Densification of firn in regions of the GrIS accumulation area that do not melt is primarily driven by overburden, with spatial variations in densification rates linked to temperature and accumulation rate [Herron and Langway, 1980]. Theoretically, the dominant densification processes with increasing depth result in order, from (1) settling (physical rounding and packing, as well as sublimation and diffusion); (2) recrystallization and deformation; (3) deformation with maximum crystal surface contact (this "creep" pushes air out of the firn), and finally (4) compression of closed-off air bubbles within the ice (which is also due to creep) [Paterson, 1994; Maeno and Ebinuma, 1983]. The densities at which the transitions between these processes occur are typically given as 550, 730, and 830 kg/m<sup>3</sup>

<sup>1</sup>Center for Geophysical Investigation of the Shallow Subsurface, Boise State University, Boise, Idaho, USA.

<sup>2</sup>Department of Geosciences, University of Montana, Missoula, Montana, USA.

<sup>3</sup>Institute of Arctic and Alpine Research, University of Colorado Boulder, Boulder, Colorado, USA.

<sup>4</sup>Department of Geology and Geophysics, University of Wyoming, Laramie, Wyoming, USA.

<sup>5</sup>Byrd Polar Research Center, The Ohio State University, Columbus, Ohio, USA.

[Paterson, 1994; Maeno and Ebinuma, 1983]. More recent studies reveal that these transition densities vary spatially and are not always identifiable in cores [Hörhold et al., 2011].

[4] However, more than 1/3 of the GrIS has net positive accumulation and receives some amount of surface melt annually [Nghiem et al., 2005]. Although this area includes both the percolation and soaked facies, as described by Benson [1960], there is no surface expression for the boundary between them; thus we refer to this area as the “percolation zone.” The size and distribution of the percolation zone is annually transient because of yearly variations in total accumulation and extent of melt. Within the percolation zone, surface meltwater infiltrates the snow layer and refreezes to form ice layers, ice lenses, and ice pipes [e.g., Benson, 1960; Pfeffer et al., 1991]. This process of melt and refreeze results in densification processes that deviate from the typical densification model for dry firn. Georadar surveys within the percolation zone reveal a layered subsurface with laterally continuous high-reflectivity horizons that are often interpreted as previous summer surfaces [e.g., Dunse et al., 2008; Legarsky and Gao, 2006]. Detailed shallow core and snow-pit studies of the upper few meters of firn within the percolation zone [e.g., Benson, 1960; Fischer et al., 1995; Parry et al., 2007; Dunse et al., 2008] reveal seasonal high-density layer boundaries. Throughout this layered structure are ice lenses and ice pipes. All of these observation techniques show increased meltwater retention with a decrease in elevation until complete saturation of the surface layer is eventually reached by the end of the melt season [Braithwaite et al., 1994].

[5] Cores collected in the upper regions of the percolation zone [e.g., Mosley-Thompson et al., 2001] span the full depth of the firn column from the annual snow layer to the theoretical firn close-off density of  $\sim 830 \text{ kg/m}^3$  [Paterson, 1994]. These cores have been used to calculate long-term average accumulation rates, density versus depth relationships ( $d\rho/dz$ ), and densification rates ( $d\rho/dt$ ). The ability to determine these rates depends on the identification of annual signals in the core. This is difficult in regions with melt because they have a more vertical dispersion of possible seasonal indicators (dust,  $\delta^{18}\text{O}$ ,  $\delta\text{D}$ , etc.) [Hou and Qin, 2002] than do regions without melt. Thus, the quality of information preserved in cores is limited where melt is substantial, and therefore cores acquired in the percolation zone are usually short and from regions with very little melt. Therefore, the effect of increased surface melt on firn densification through the entire firn column is largely unknown. This is especially true at lower elevations of the percolation zone.

[6] Common midpoint (CMP) georadar surveys have been used to estimate the average electromagnetic (EM) propagation velocity as a function of depth for the firn column in the dry snow zone of the GrIS [e.g., Hempel et al., 2000]. Where the focus of these surveys is to match common offset radar reflection horizons with contemporaneous features in ice cores [e.g., Hempel et al., 2000], it is common to treat the firn column as a single layer and determine the normal moveout (NMO) stacking velocity ( $\nu_{\text{NMO}}$ ) of the firn column, which closely approximates the root-mean-square (RMS) velocity ( $\nu_{\text{RMS}}$ ) in a horizontally layered homogeneous

medium [Yilmaz, 2001]. There are many methods for calculating  $\nu_{\text{NMO}}$ . The most precise method is to pick traveltime versus offset curves along the first break of a coherent reflection and linearly fit the resultant curve in the time-squared versus distance-squared domain; however, semblance analysis is most often used to determine  $\nu_{\text{NMO}}$ . In a multilayered system, there are also many methods for calculating the average velocity of each layer, or interval velocity. The Dix inversion, which solves for layer velocities using only stacking velocities and zero-offset traveltimes [Dix, 1955], is the most common method of calculating interval velocities.

[7] Here we use CMP georadar surveys to calculate how firn column density varies with depth at 13 locations along the Expédition Glaciologique Internationale au Groenland (EGIG) line within the percolation zone of the GrIS. We collected our data in the summers of 2007 and 2008 in an area that spans  $\sim 70 \text{ km}$  laterally and  $600 \text{ m}$  of elevation (1997 to 1401 m) from Crawford Point toward Swiss Camp (Figure 1). We avoid the NMO analysis and Dix inversion method for two reasons: (1) Dix inversion is subject to assumptions of NMO, which include small offset-to-depth ratios and small velocity gradients over reflection boundaries [Bradford, 2002], and (2) Dix inversion is sensitive to small errors in NMO velocity and near-offset traveltime picks. Instead, we employ the traveltime inversion method of Zelt and Smith [1992], which is not subject to the assumptions of NMO. We follow a set of explicit rules to solve for the electromagnetic (EM) velocity structure of the firn column. We create and follow an inversion flow (Figure 2) to find the simplest velocity versus depth model that describes the data within estimated uncertainty, reduces sensitivity to small errors in velocity, and limits user bias, and to give a basis for evaluating how well our results fit the data in the context of physically realistic firn density models. Our method has four steps: (1) picking time versus offset moveout curves from georadar data, (2) using a traveltime inversion to invert for a one-dimensional depth-velocity model, (3) checking the solution with forward modeling for quality control (QC), and (4) solving for layer density from radar velocity. Our method allows us to calculate the density profile for the entire depth of the firn column at all locations in this survey. We include comparisons with a firn compaction model that neglects the influence of melt [Herron and Langway, 1980] at every location and with core data at Crawford Point.

[8] Radar propagation velocity in dry snow primarily depends on snow density [Tiuri et al., 1984]. However, radar velocity in the presence of liquid water is a function of both density and volumetric water content [e.g., Bradford et al., 2009]. Temperature data during the 9 days of data collection indicate that surface melt likely occurred at some sites during data collection in the 2007 field season (Table 1). Indeed, surface snow was noticeably wet at T1, T2, and T3; small amounts of liquid water may also have been present near the surface at T4, T5, and Crawford Point when we collected data. We drilled firn cores to  $\sim 10 \text{ m}$  depth at the midpoint of each CMP. Each core had evidence of past melt and refreeze such as ice lenses and ice pipes throughout the core. However, these cores did not show evidence of liquid water. Furthermore, measured  $10 \text{ m}$  depth firn temperatures were between  $-16^\circ\text{C}$  and  $-3^\circ\text{C}$ . Thus we assume that the

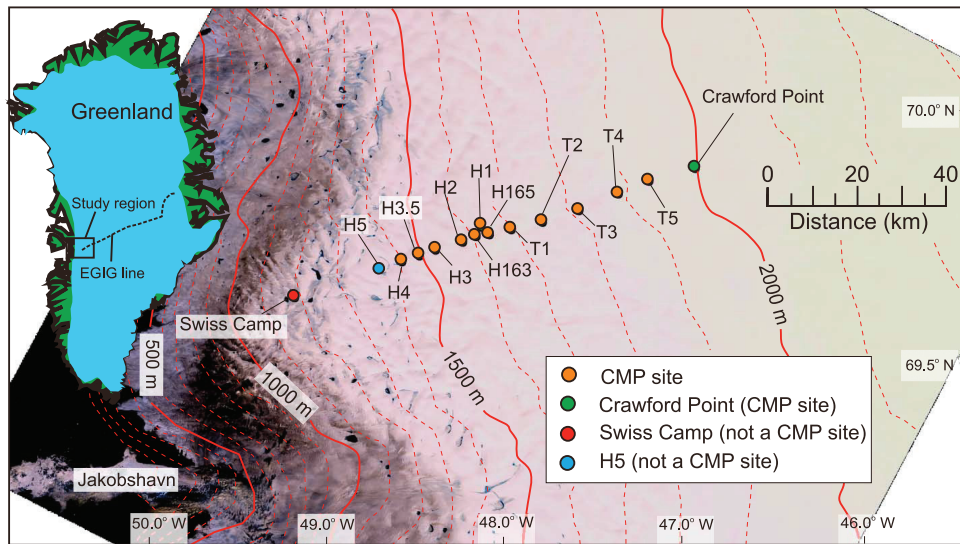


**Figure 1.** Advanced Spaceborne Thermal Emission and Reflection Radiometer (ASTER) image with CMP radar sites marked. The Expédition Glaciologique Internationale au Groenland (EGIG) line and the approximate location of the ASTER image are marked on the map of Greenland. Red elevation contours are approximated from 5 km gridded elevation data [Bamber *et al.*, 2001].

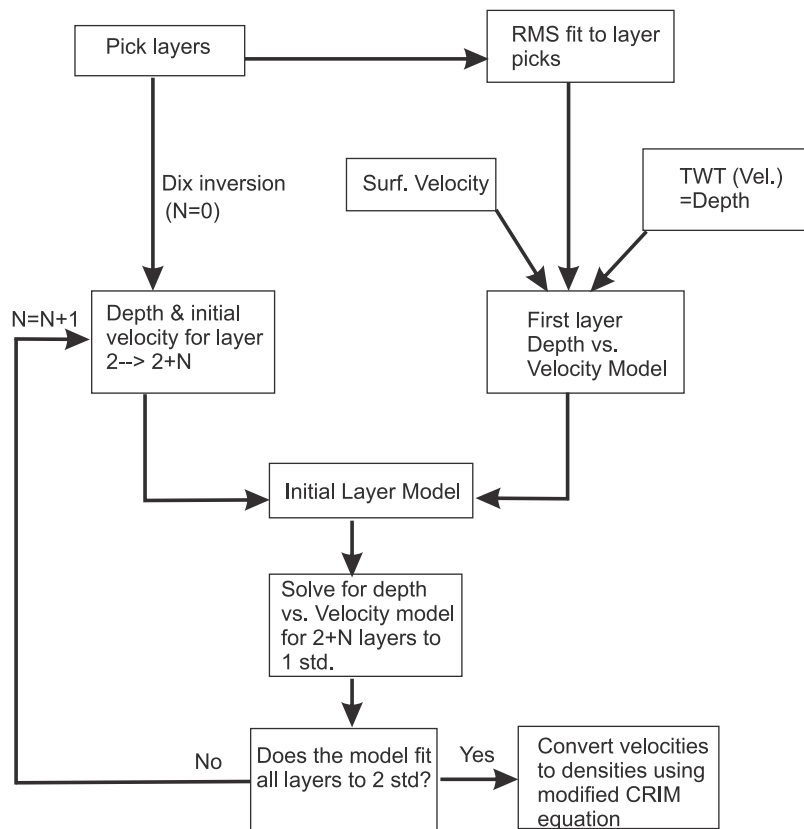


**Figure 2.** Flowchart for the inversion process.

**Table 1.** Site Locations, Depth to 830 kg/m<sup>3</sup>, Date of Data Collection, and Temperature Data for Day of Data Collection<sup>a</sup>

Site Name	Latitude	Longitude	Elevation (m)	Depth to 830 (m)	Date of Data Collection	Average Temperature on Date of Data Collection (°C)
Crawford Point	69.87650	47.01020	1997	58	26 Jun 07	0
T5	69.84802	47.27358	1932	71	7 Jul 07	-0.3
T4	69.81998	47.45050	1877	69	3 Jul 07	-2.9
T3	69.78360	47.67018	1819	63	3 Jul 07	-2.5
T2	69.75693	47.88028	1750	58	28 Jun 07	0.5
T1	69.73802	48.06097	1710	67	28 Jun 07	0.8
H165	69.72505	48.19020	1660	43	21 May 08	-19.0
H1	69.73908	48.24030	1680	25	16 May 08	-10.9
H163	69.71978	48.26740	1644	18	22 May 08	-14.8
H2	69.70617	48.34497	1555	28	31 May 08	-9.3
H3	69.68743	48.49967	1540	26	18 May 08	-7.6
H3.5	69.67393	48.59112	1497	14	31 May 08	-8.9
H4	69.66018	48.68945	1401	3	22 May 08	-13.0

<sup>a</sup>The temperature data are an average of air temperature readings from four instruments at Crawford Point, which are part of the Greenland Climate Network [Steffen *et al.*, 1996]. The average air temperature is the mean value of the readings for the full diurnal cycle during the day of data collection at Crawford Point with a temperature lapse rate of  $-7.4^{\circ}\text{C}$  per 1000 m rise in elevation [Hanna *et al.*, 2005].

amount of deeply infiltrating liquid water at any given time in any given location is negligible.

## 2. Methods

### 2.1. Data Acquisition

[9] We used a Sensors and Software pulseEKKO PRO georadar system with 100 MHz antennas. Our offset range was 1–80 m with a moveout interval of 0.8 m in 2007 and 0.5 m in 2008. We recorded for 1820 ns per trace, but coherent reflections were not apparent below 1500 ns. For processing, we assumed that firn layers were laterally homogeneous and parallel over the length scale of the moveout profiles at each site. However, shallow core (10 m) and common-offset data revealed that layering is not

laterally homogeneous and density varied by an average of 20% over the depth of the cores at Crawford Point ( $\sim 1997$  m above sea level (asl)) and by 2% at H1 ( $\sim 1680$  m asl) [Brown *et al.*, 2011]. Fortunately, lateral density variations decreased with depth. Furthermore, the length scale of lateral density variations is small ( $<5$  m) and therefore averages out over the width of the CMP. The amplitude of surface roughness from sastrugi was less than  $\sim 0.2$  m over the 80 m offset. This roughness causes a waviness in the direct subsurface wave, either through variation in the propagation velocity or scattering that interferes with the direct wave (Figure 3b). However, linear fits to the direct subsurface wave produced surface velocity estimates with standard deviations of less than  $\pm 0.003$  m/ns at most locations.

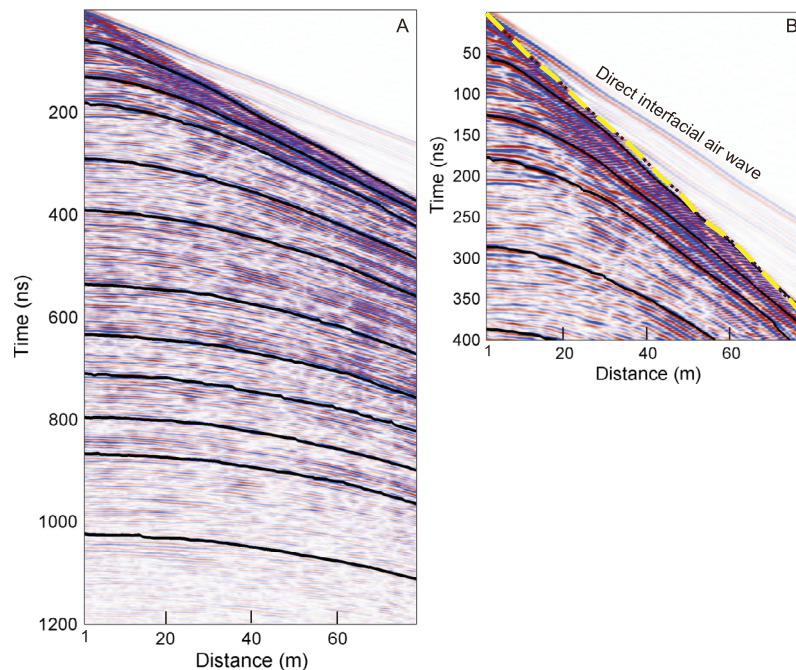


**Figure 3.** (a) Example of georadar common midpoint (CMP) data with picks (black lines) from T5. (b) A magnified view of the upper 400 ns reveals the waviness of the direct subsurface wave (yellow and black dashed line).

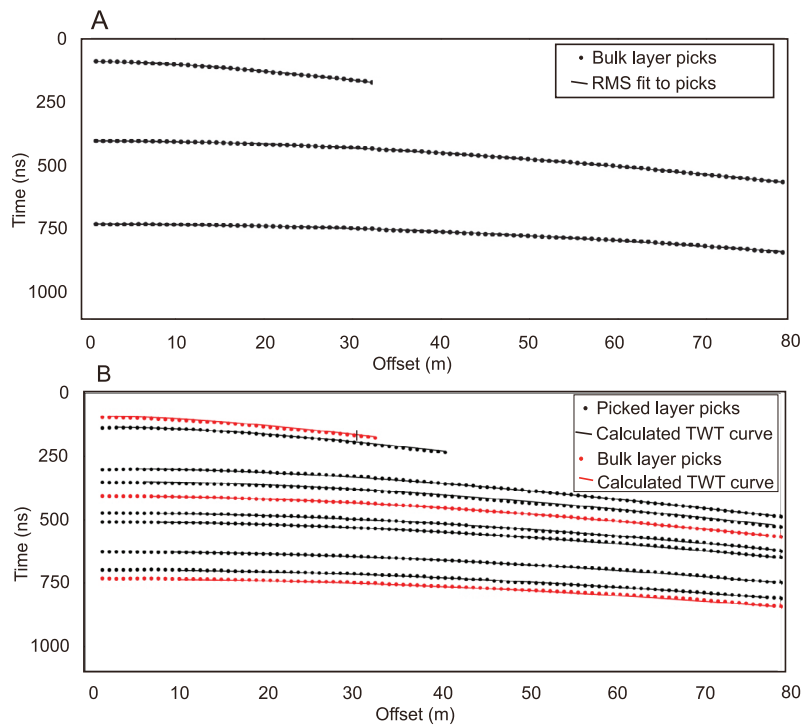


**Figure 4.** (a) Bulk layer picks from Crawford Point CMP data with RMS fit. (b) Modeled TWT fit to all picked layers (both black and red) at Crawford Point. Bulk layers used for the inversion are shown in red.

Because dip slopes and the slopes of the sastrugi were small, residual moveout errors are negligible.

## 2.2. CMP Surveys

[10] Figure 3a shows a common midpoint radar profile with handpicked moveout curves superimposed. Data processing included a time-zero shift to correct for trace start time delay and traveltime drift with temperature in the electronics, a 25–50–200–400 MHz Ormsby band-pass filter to reduce low- and high-frequency noise, and a time-variable gain function of  $t^{1.2}$  to compensate for attenuation that is due to absorption and spherical spreading. We picked moveout curves using a semiautomatic picking routine in ProMAX (seismic processing software from Halliburton) that identifies the peak in the wavelet closest to a handpicked point. We then adjusted our picks to that of the first break of the wavelet to account for the finite bandwidth of the signal. Because shallow moveout curves are dominated by direct subsurface waves at long offsets, we limited our picks to offsets smaller than that at which the reflections merge with the direct subsurface wave. For each location we picked traveltime versus offset data for as many coherent (constant relative phase of waveform) reflections as were present in the data, up to a total of 11. The shape of the traveltime curves is a function of the depth to the boundary causing the reflection and the velocity of all overlying material.

## 2.3. Velocity Versus Depth

[11] We employ the method of *Zelt and Smith* [1992] to solve for the velocity versus depth structure of the firn column. The method utilizes a ray-based forward model to

compute traveltimes coupled with a damped least squares inversion algorithm to find the layered velocity model that produces the best fit to traveltime picks within the CMP data. As with all velocity estimation methods, traveltime inversion is nonunique. Therefore we developed rules to ensure that the inversion procedure was consistent across all sites with an end objective of comparing relative variations in the final density versus depth models.

[12] The rules constrain nonuniqueness in the inversion by iteratively solving for the depth and propagation velocity rather than solving for both simultaneously. Further, instability of the inversion increases as the number of layers increases and as the thicknesses of the layers decrease; therefore we chose to solve for the simplest model that describes all of the traveltime picks to within a specified uncertainty threshold (Figure 4).

[13] Here we define two categories of model layers: (1) “picked layers,” for which we use models that include a layer for each picked moveout curve; and (2) “bulk layers,” for which we use models that combine picked layers into groups. We use the term *layers* to describe generalities that apply to both picked layers and bulk layers. We ran our inversion on bulk layers, which combine multiple picked layers into a single layer. We then checked the quality of our fit to all of the picked layers (Figure 4).

[14] We ran our inversion twice for each site, assuming different velocity profiles with depth. One set of inversions was run assuming that EM propagation velocity decreases linearly with depth through a single bulk layer and that inflections in the velocity versus depth curve occur at

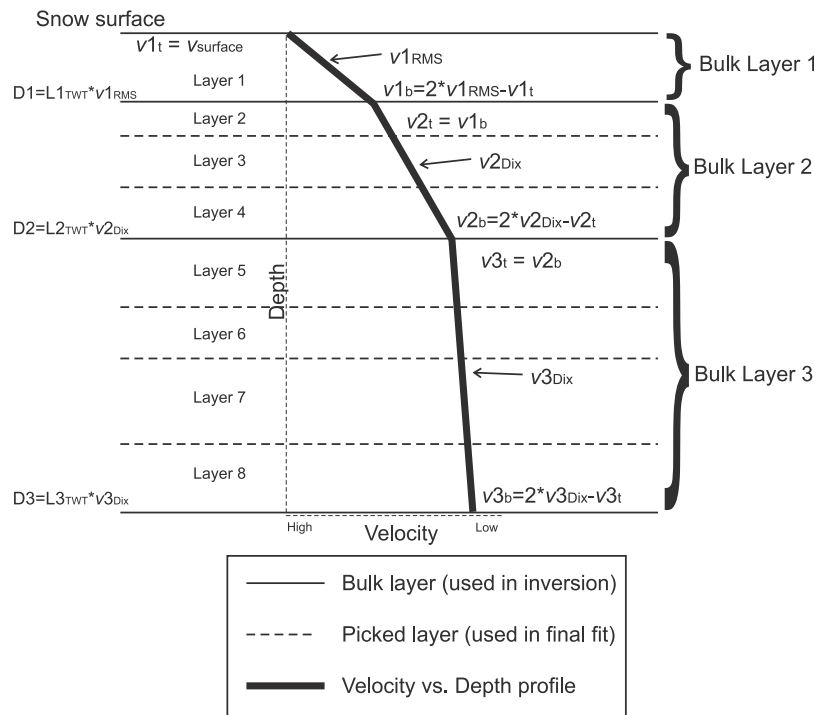


**Figure 5.** Schematic showing the model velocity versus depth curve for the linear gradient inversion. The model includes multiple picked layers for each bulk velocity layer. How velocity and depths are determined is described in the appendix.

boundaries between bulk layers (Figure 5). Hereafter, we refer to this method as the “linear gradient inversion.” A single linear velocity gradient across many picked layers is based on the assumption that the dominant densification processes follow the typical dry-firn densification processes described in the Introduction. However, the relationship between radar propagation velocity and firn density (described in section 2.4) is not linear. The error in calculated density values that is due to this nonlinearity increases with depth to  $\sim 8\%$  at 80 m. Because of this systematic error we applied a second inversion in which we assumed that the subsurface can be modeled as a stack of constant velocity bulk layers (Figure 6). This inversion (hereafter called the “stepped velocity inversion”) assumed stepwise linear changes in density in which the estimate is the mean density for the entire bulk layer.

[15] Each inversion required a starting velocity model that we calculated directly from the CMP traveltimes picks. We adjusted the profile of EM propagation velocity with depth systematically until rays traced through the model fit the traveltimes picks to within a specified uncertainty threshold. We solved for one bulk layer boundary at a time, and for the velocity-depth profile from top to bottom, sometimes referred to as layer stripping. All shallower bulk layers must meet the fitting criteria before solving for the next bulk layer. This process resulted in an internally consistent inversion procedure that allowed us to compare depth-density curves between CMP sites. It is important to note that following the rules described in the appendix produces equally good fits to the data for either inversion procedure.

## 2.4. Density From Velocity

[16] Within the ice-air-water-vapor system that makes up the firn column, only ice, air, and water greatly influence the propagation velocity ( $\nu$ ) of the radar pulses. Impurities account for a very small volume percentage and thus can be ignored when calculating propagation velocities in firn. Water, air, and ice have negligible conductivities and magnetic permeabilities ( $\mu$ ) very close to that of free space ( $\mu_0$ ); they largely differ in relative dielectric permittivity ( $\epsilon_r$ ). The radar signal velocity is  $\nu = \frac{c}{\sqrt{\epsilon_r}}$ , where  $c$  is the speed of light. As stated in the Introduction, we assume that the amount of liquid water at any given time in any given location is negligible. Thus, we assume that the firn is composed entirely of ice and air. This assumption is not always valid in the percolation zone. For example, if there is a large amount of melt before or during the georadar survey (such as occurred for sites T1, T2, and T3), the near-surface layer(s) will have liquid water present. Even small volumetric water contents (less than 0.1) can change propagation velocities by more than 15% compared with dry snow of the same density [Bradford *et al.*, 2009].

[17] When we can neglect effects of liquid water we are left with a two-phase system in which cold ice and air are the only contributors to bulk dielectric properties. The interaction of the radar signal with this mixture is affected both by the volumetric ratio of ice to air as well as by the shape and orientation of the ice crystals and air voids. However, Harper and Bradford [2003] show that, for cold snow, the complex refractive index model (CRIM) equation [Wharton *et al.*, 1980; Knight *et al.*, 2004] can be adapted to closely

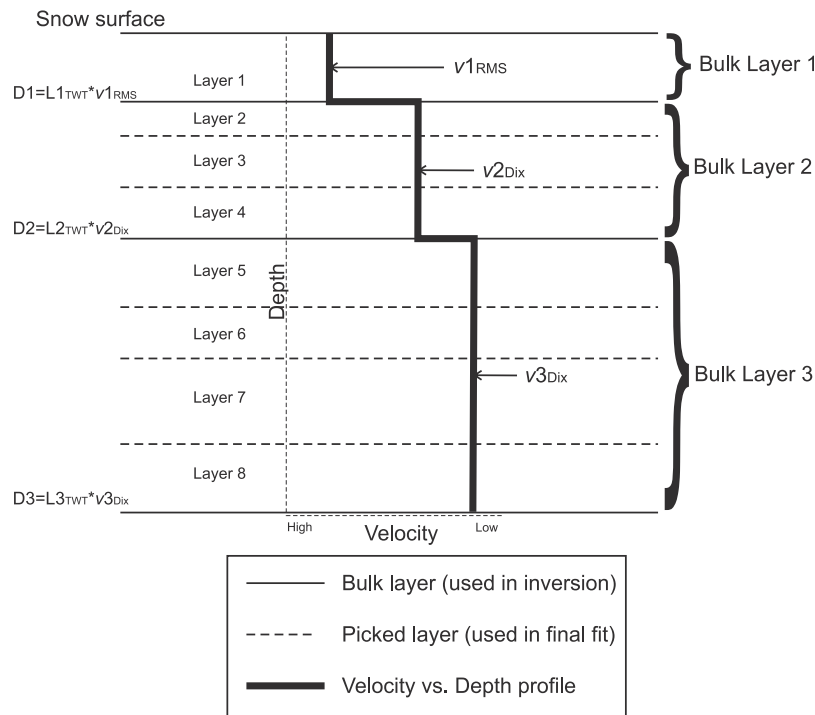


**Figure 6.** Schematic showing the model velocity versus depth curve for the common velocity inversion. The model includes multiple picked layers for each bulk velocity layer. How velocity and depths are determined is described in the appendix.

estimate the bulk density of the mixture based on the velocity of the EM wave propagation. The adapted CRIM equation is

$$\rho_f = \left( \frac{v_a/v_f - 1}{v_a/v_i - 1} \right) \rho_i,$$

where  $\rho_f$  and  $\rho_i$  are the densities of firn and ice, respectively, and  $v_f$ ,  $v_i$ , and  $v_a$  are the EM propagation velocities of firn, ice, and air, respectively.

## 2.5. First-Order Density Model

[18] We compared our estimated density profiles with hypothetical density profiles that assume no melt infiltration and refreeze. To do this, we calculated simplified depth-versus-density curves using the empirically based model of *Herron and Langway* [1980] (the HL model), a first-order estimate of the density profile in dry conditions. By comparing our georadar-derived densities to density profiles calculated with the HL model, we obtained a sense of how melt affects firn density through the entire firn column. The HL density curve depends on the 10 m firn temperature, the accumulation rate, and the initial snow density. We assumed that the 10 m firn temperature represents the mean annual air temperature at Crawford Point. Under this assumption we used the average surface temperature of  $-16.85^\circ\text{C}$  measured at Crawford Point [*Fausto et al.*, 2009] and applied a temperature lapse rate of  $-7.4^\circ\text{C}$  per 1000 m [*Hanna et al.*, 2005] rise in elevation to calculate the relative 10 m core temperatures that are expected for the other sites. For the model accumulation rate at all locations we used the average

accumulation rate of 0.46 m of water equivalent measured at Crawford Point (E. Mosley-Thompson, unpublished core data), which agrees well with previous measurements of accumulation at Crawford Point [e.g., *McConnell et al.*, 2000; *Bales et al.*, 2009]. Although the mass balance varies greatly over the length of our transect, the greatest part of this variation is due to summer melt. *Box et al.* [2004] show that over the span of our transect the accumulation varies by approximately 0.04 m water equivalent ( $\sim 7.8\%$ ). For all locations we assume an initial snow density of  $375 \text{ kg/m}^3$  [*Braithwaite et al.*, 1994].

## 3. Results

### 3.1. Accuracy of the Method

[19] To validate the accuracy of our method, we compared the results of both inversions of georadar data collected at Crawford Point with a 120 m core drilled in the same year within 1 km of our CMP (Figure 7). We identified 10 continuous reflections within the Crawford Point radar data. The linear gradient inversion required three layers to achieve a good fit to all traveltime picks. The stepped velocity inversion required two layers. Because it represents layer average velocity, the stepped velocity inversion is best represented by two depth-versus-density points plotted at the mean depth of the corresponding layer. Both estimates lie within the core measurements acquired at Crawford Point (Figure 7).

[20] We estimated the variability within the core data by fitting the core density versus depth data with a second-degree polynomial. The  $2\sigma$  value of the residuals from the second-degree polynomial fit to the data is  $\sim 48 \text{ kg/m}^3$ . We

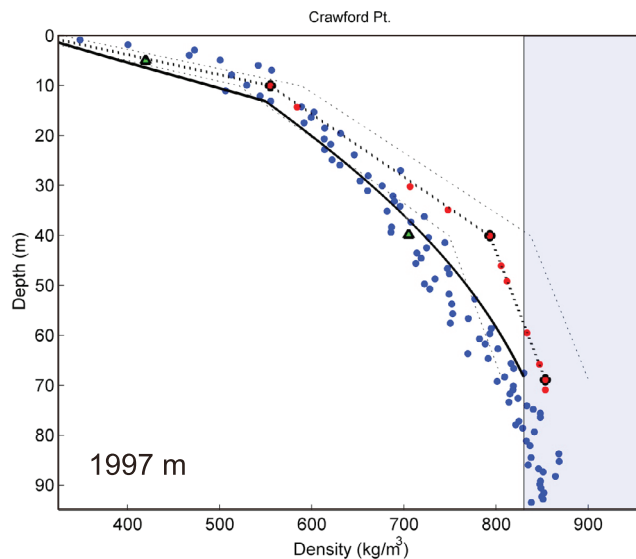


**Figure 7.** Georadar- and core-derived depth-versus-density profiles for Crawford Point. The blue dots show the measured core density-versus-depth values. The red dots connected by dashed black line show the linear gradient inversion. The red dots with black outline show the bulk layer solutions. The thin black dashed lines show the error bounds, which are based on a velocity range of  $\pm 0.002$  m/ns for each modeled layer. The green triangles show the stepped velocity inversion. The solid black curve shows the dry snow density curve calculated with the HL model. The elevation of Crawford Point is shown in the lower left-hand corner. The light blue region represents ice (density  $\geq 830$  kg/m<sup>3</sup>). Georadar and core values were obtained within 1 km of Crawford Point but are not from the exact same location.

also estimate the variability within the core data by fitting linear segments to the core density versus depth data. We divided the data into three theoretical densification regimes: (1) less than 550 kg/m<sup>3</sup>; (2) 550–830 kg/m<sup>3</sup>; and (3) above 830 kg/m<sup>3</sup>. The  $2\sigma$  value of the residuals from these fits is  $\sim 37$  kg/m<sup>3</sup>. We chose to compare our results with this second fit to the core data because the residuals are less than the second-degree polynomial fit. The linear gradient inversion result is best represented by three segments that connect four depth-versus-density points. If we assume that our inversion fits the velocity data within 0.002 m/ns ( $\sim 1\%$ – $1.5\%$  of the velocities measured), the associated density variation is between 26 and 49.6 kg/m<sup>3</sup> for a density of 340 and 917 kg/m<sup>3</sup>, respectively. We assume this error because the associated density values are approximately equivalent to the natural variability in density found in the core. Using this range as error bounds for our inverted data, we find that the core data variability overlaps the error of the radar-derived data (Figure 7). Last, the HL model falls within the range of measured core densities.

### 3.2. Density Versus Depth Profiles Along the EGIS

[21] We determined linear gradient and stepped velocity models for all 13 locations between Crawford Point and site

H4 (Figure 7–Figure 10), along with the HL modeled density profiles (zero-melt assumption). Both inversions show that the density increases with depth at a greater rate as elevation decreases. From Crawford Point to site H165, the curves generally follow the HL model (Figure 7–Figure 9b). The density versus depth curves for sites H1 and H163 appear bimodal (Figures 9c and 9d). At both locations our results show a low-density layer less than 10 m thick overlying an ice layer that we identify at a depth of  $\sim 27$  and  $\sim 19$  m for sites H1 and H163, respectively. As the transect continues through lower elevations, the density profiles continue to have higher densification rates until, at H4, there is a thin, low-density surface layer directly overlying ice (Figure 10).

[22] We calculated the depth to the close-off density (830 kg/m<sup>3</sup>) for our linear gradient profiles (Figure 11, diamonds) and for the HL modeled density curves (Figure 11, squares). We assume that the depth to close-off is the effective depth of the firn column. We also calculated the ice-equivalent depth of the firn column for each location (Figure 11, triangles). The HL model close-off depths and the radar-derived close-off depths are within 10 m for Crawford Point through T1. At H165, the close-off depth calculated from the HL model and the close-off depth calculated from our measurements start to diverge significantly; our measurements show close-off at  $\sim 43$  m whereas the HL model predicts close-off at 62 m. The sites between H1 and H4 all have close-off depths that are less than half the depth calculated with the dry conditions assumed in the HL model.

## 4. Discussion

### 4.1. Methods

[23] Further justification for our departure from the standard semblance analysis or Dix inversion method of inverting for the velocity structure of the firn column is necessary. In the Introduction we list two reasons that we chose not to use the common semblance analysis or Dix inversion method. The first is that the Dix inversion is subject to assumptions of NMO, whereas our method is not. The NMO assumptions of small offset-to-depth ratios and small vertical velocity gradients [Bradford, 2002] are violated in our surveys. The assumption of small offset-to-depth ratios is violated in the upper firn layers at all of our CMP sites. The assumption of small vertical velocity gradients is clearly violated at some of the lowest CMP sites, where densities increase by  $\sim 50\%$  in less than 10 m depth (i.e., Figure 10, site H3.5). The second reason we chose not to use the common semblance analysis or Dix inversion method is that the Dix inversion is sensitive to small errors in velocity. Systematic errors in velocity measurements can occur by picking the semblance at the wave peak, which is especially true for shallow reflections. True velocity estimates come from the moveout of the first break of the wavelet, which does not produce a semblance response [Murray et al., 2007]. This is because semblance is a measure of multioffset coherence of wave phase, which is zero at the first break of the wavelet. Further, we do not have a direct physical comparison to determine the accuracy of our results for most of our CMP sites. Thus, we chose our

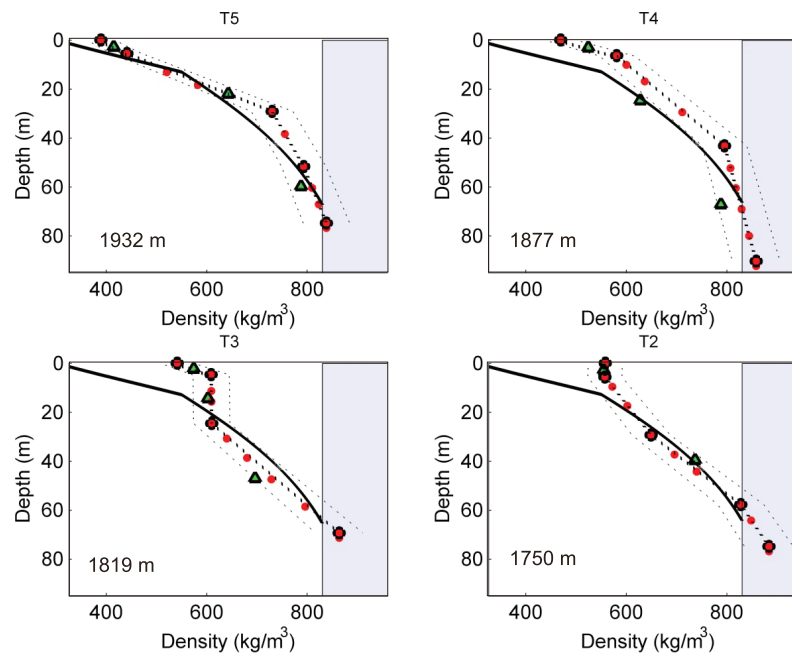


**Figure 8.** Georadar-derived depth-versus-density profiles for T5, T4, T3, and T2. The red dots connected by dashed black line show the linear gradient inversion. The red dots with black outline show the bulk layer solutions. The thin black dashed lines show the error bounds, which are based on a velocity range of  $\pm 0.002$  m/ns for each modeled layer. The green triangles show the stepped velocity inversion. The solid black curves show dry snow density curves for the HL model. The numbers in the lower left-hand corner indicate site elevations. The light blue region represents ice (density  $\geq 830$  kg/m<sup>3</sup>). Note that it is likely that the surface layer densities for T3 and T2 are inaccurately high due to the presence of small amounts of liquid water near the surface.

inversion methods because they allow us to systematically solve for change in density with depth by using a consistent set of rules.

[24] Our methods of inverting for radar velocities do not determine specific annual layer densities. Instead, we either calculated average densities or density gradients through many annual layers. Within each inversion method, our procedure provided the simplest model that describes the observed traveltimes to within an accuracy threshold justified by the data. The scale of the measurement is much greater than the scale of ice lenses, ice pipes, and sastrugi, so that the average densification rate in depth is determined over a large area and corresponding firn volume. Determining the densification rate over a large area and through multiple annual layers gives a more general picture.

[25] The two inversion methods that we describe in Appendix A differ in the basic representation of the model subsurface. The stepped velocity model has an average velocity for each layer with a velocity step at each layer boundary. It is best represented by a single density versus depth point for each layer, the depth of which is the average depth of the layer. Of the 13 sites, we fitted the CMP picks at 6 sites with a two-layer solution, with a three-layer solution at 6 sites, and with a four-layer solution at only 1 site (Figure 9, site H165). We show in Figure 7 that the inversion fits the core density at Crawford Point, although the two points that define the subsurface model do not show the shape of the densification curve. So, although the stepped velocity inversion is accurate, 12 of the 13 solutions

define the density-versus-depth curve with only two or three points.

[26] The linear gradient model provides a continuous velocity curve with a velocity gradient change at each bulk layer boundary. Each picked layer within the bulk model layer defines a depth-versus-density point along the curve. We fitted the CMP picks at 3 sites (H2, H3, and H4) with a two-layer solution (Figure 10), a three-layer solution at 7 sites, and a four-layer solution at 3 sites. The fit to the core data at Crawford Point is not as good for the linear gradient inversion as it is for the stepped velocity inversion, but the fit is within the estimated error of our inversion. Further, more than 80% of the depth-versus-density points calculated with the stepped velocity model fall within the error estimate of the curve calculated with the linear gradient inversion.

[27] The differences in the final velocity models indicate the inherent nonuniqueness in the problem and also indicate the uncertainty in the solution. We can compare the relative density profiles of all sites with no a priori knowledge of the subsurface because our inversions are consistent across all locations. However, the density with depth values calculated with the linear gradient inversion are valid at all of the picked layer depths, whereas the stepped velocity model represents only the mid-depth point of each bulk layer. Thus, although the two methods produce an equally good fit to the data, we used the linear gradient inversion to investigate changes in firn depth and depth-versus-density curves across our study area.

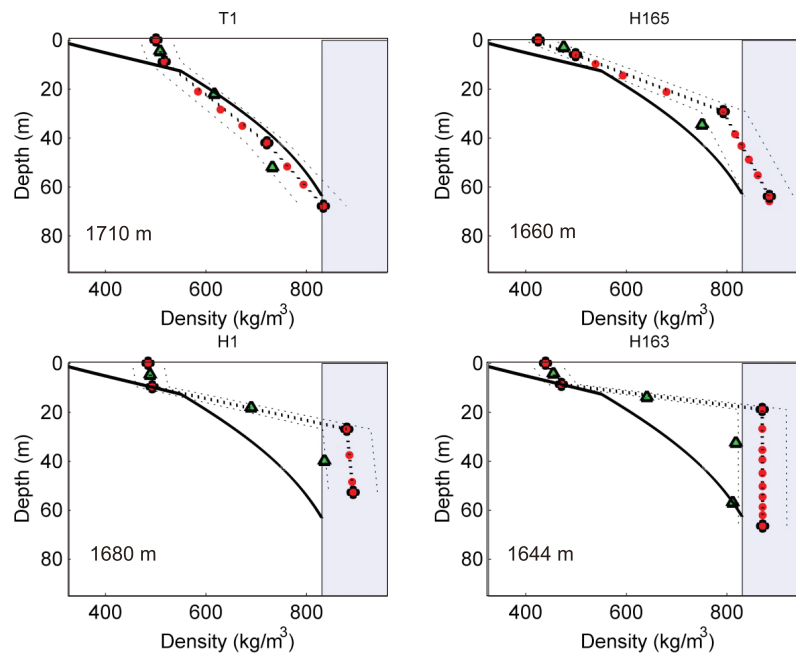


**Figure 9.** Georadar derived depth-versus-density profiles for T1, H165, H1, and H163. The red dots connected by dashed black line show the linear gradient inversion. The red dots with black outline show the bulk layer solutions. The thin black dashed lines show the error bounds, which are based on a velocity range of  $\pm 0.002$  m/ns for each modeled layer. The green triangles show the stepped velocity inversions. The solid black curves show dry snow density curves for the HL model. The numbers in the lower left-hand corner indicate site elevations. The light blue region represents ice (density  $\geq 830$  kg/m<sup>3</sup>). Note that it is likely the surface layer density for T1 is inaccurately high due to the presence of small amounts of liquid water near the surface.

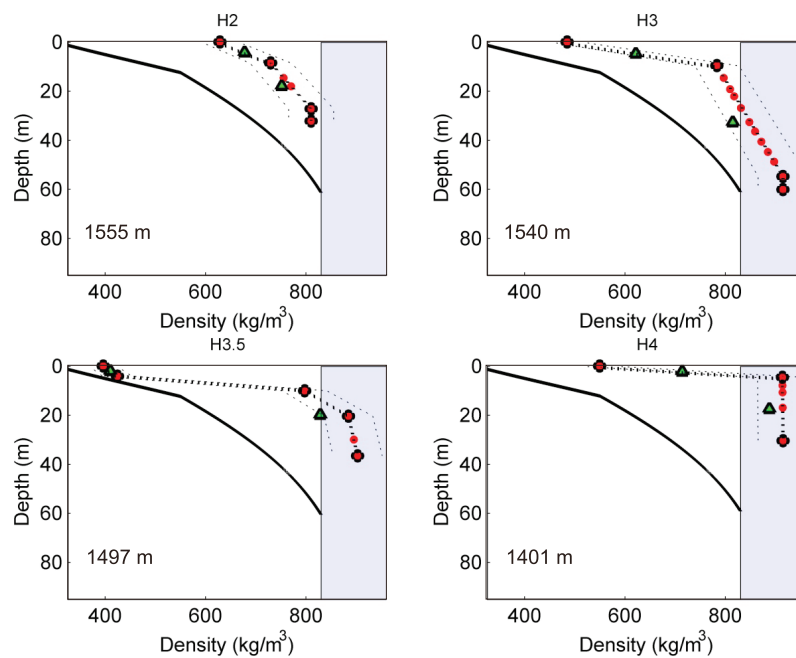


**Figure 10.** Georadar-derived depth-versus-density profiles for H2, H3, H3.5, and H4. The red dots connected by the dashed black line show the linear gradient inversions. The red dots with black outline show the bulk layer solutions. The thin black dashed lines show the error bounds, which are based on a velocity range of  $\pm 0.002$  m/ns for each modeled layer. The green triangles show the stepped velocity inversions. The solid black curves show dry snow density curves for the HL model. The numbers in the lower left-hand corner indicate site elevations. The light blue region represents ice (density  $\geq 830$  kg/m<sup>3</sup>).

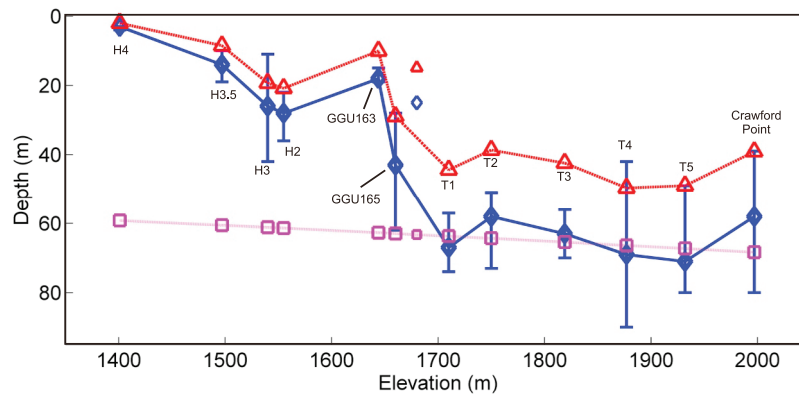


**Figure 11.** Depth to ice density ( $830 \text{ kg/m}^3$ ) versus elevation for all locations, as determined with georadar (blue diamonds) and calculated with HL model (pink squares). The ice-equivalent depth is indicated with red triangles. Error bounds for depth to  $830 \text{ kg/m}^3$  are the limits encompassed by the error estimates shown in Figure 7–Figure 10 (dashed lines).

[28] As we stated in section 3.1, the fit between the density profile derived from the linear gradient inversion and the core density profile at Crawford Point is not perfect. Inversion of the georadar data for density is not unique; thus we do not necessarily expect an exact match. In fact, by including more layers in our inversion, we could substantially improve the fit. However, we would risk biasing our inversion (manually adjusting the result to fit a preconceived density versus depth curve) or overfitting the data (fitting the noise in the data).

[29] Although we do expect the first-order shape of the georadar-derived density profile to be similar to the core depth-versus-density curve, we do not expect that our results will exactly match the core data for three reasons: (1) the data are not from the same exact location, (2) our method does not solve for exact densities of each layer but instead solves for the large-scale densification trend over multiple years of accumulation, and (3) the core lengths for which density was measured and the CMP radar survey measure very different volumes. A 9 cm diameter core samples  $\sim 1 \text{ m}^3$  within the upper 80 m of firn, whereas our data represent  $\sim 1500 \text{ m}^3$  of firn to 80 m at our maximum offset. This estimate assumes that the zone of influence of the radar signal is  $\sim 0.5 \text{ m}$  wide and that the radar signal travels the shortest distance path to 80 m depth at 80 m offset. In the upper regions of the percolation zone, the relatively large volume of firn measured by our methods resulted in a density profile that more likely represents the surrounding  $1 \text{ km}^2$  than do individual cores, which can vary greatly over short distances [Brown *et al.*, 2011]. However, our method cannot resolve the short-scale density variability that is apparent in the core data.

[30] It is important to acknowledge that the calculated densities for layers with liquid water present are inaccurate, which includes the surface layers for T1, T2, and T3. However, measurements of velocity in these upper layers are valid; thus they do not produce a measurement error that could propagate through the rest of the inversion. Instead, errors introduced by liquid water content near the surface influence the calculation of the density only in the top layer; all other layer densities are accurate to the same error bounds as regions with no liquid water in the surface layer.

## 4.2. Density Profiles

[31] Our radar-based calculations of pore close-off depth ( $830 \text{ kg/m}^3$ ) (Figure 11, diamonds) show a slowly diminishing depth to ice at  $830 \text{ kg/m}^3$  as elevation decreases from Crawford Point to T1, a sharper decrease in depth to  $830 \text{ kg/m}^3$  between T1 and H163, and another region of slowly diminishing depth to  $830 \text{ kg/m}^3$  as elevation decreases between H2 and H4. Our sites spanned about 600 m of elevation and encompassed areas with different amounts of melt (Figure 12). The density profiles are generated over multiple years by the combination of melt-induced densification and non-melt-induced densification (including settling, sintering, and recrystallization). *Herron and Langway* [1980] argue that as firn becomes denser with time and burial, “the proportional change in airspace is linearly related to change in stress due to the weight of overlying snow.” Although density with depth is influenced by melt at all locations along our transect, it is reasonable to conclude that overburden is the primary driver of densification where densification rates and depth to  $830 \text{ kg/m}^3$  closely match those of the HL model. Conversely, where densification rates and depth to  $830 \text{ kg/m}^3$  deviate greatly from those of the HL model, densification is primarily driven by a surface melt infiltration and subsequent refreeze.

[32] Determining the primary driver of densification at each location allows us to assess the relationship between surface melt days, primary driver of densification, and firn density profiles, constrained by the coarse resolution of satellite-based melt day measurements. Near Crawford Point there were an average of 12.8 melt days per year with a range of 0–48 melt days per year between 1979 and 2007 (Figure 12) [Abdalati, 2007]. Near T2, melt increases to an average of 22.8 melt days per year with a range of 0–61 between 1979 and 2007. However, between Crawford Point and T1, the HL model closely approximates the calculated density versus depth profile. Thus, in this region, surface melt infiltration or refreeze does not significantly affect firn density. Near H2 there is a consistently larger number of melt days per year, with an average of 53.0 melt days per year and a range of 16–85 between 1979 and 2007

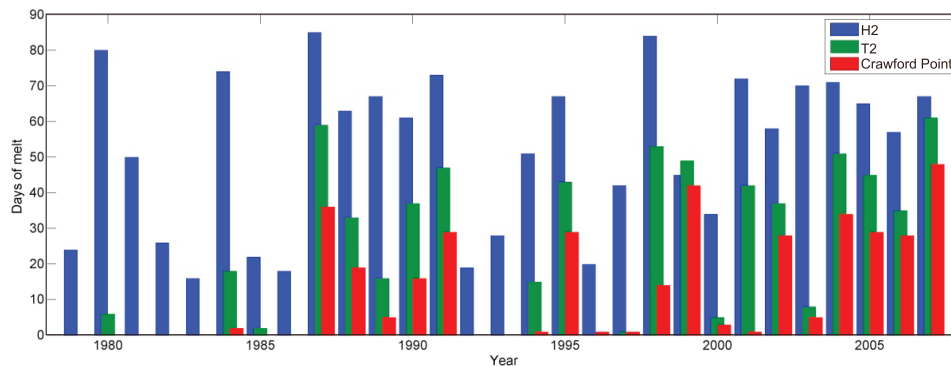


**Figure 12.** Melt days per year from 1979 to 2007 [Abdalati, 2007] for the areas around Crawford Point, T2, and H2.

[Abdalati, 2007] (Figure 12). From H2 to H4, the density versus depth profiles deviate greatly from those of the HL model (Figure 10) and depths to  $830 \text{ kg/m}^3$  are  $\sim 50\%$  of those predicted by the HL model (Figure 11). In this region, surface melt, infiltration, and refreezing dominate the densification process. The sharp decrease in depth to  $830 \text{ kg/m}^3$  between T1 and H163 reveals a relatively small transition zone between areas where firn densification is dominated by overburden and areas where firn densification is dominated by melt processes. The short distance (and corresponding elevation range) between areas may indicate that the system is sensitive to small changes in surface melt rates.

## 5. Conclusions

[33] Our methods of inverting for firn density from georadar data result in accurate density versus depth curves in firn. Our inversions for density at Crawford Point agree with core data within estimated uncertainty. Further, because there is little user bias to our inversions, it is possible to compare the resultant density versus depth profiles from multiple sites with each other. Where even small amounts of liquid water are present in the firn column, the density calculation is inaccurate. However, because the velocity inversion is layer based and gives accurate average velocities for each layer, inaccuracies that are due to liquid water at or near the surface do not propagate through the inversion.

[34] From Crawford Point to T1 (1997 to 1710 m above sea level) overall densification processes are not greatly affected by surface melt infiltration or refreeze; overburden is the primary driver of densification. From H2 through H4 (1555 to 1401 m above sea level) surface melt is the primary driver of densification. The boundary between these regions spans  $\sim 60$  m of elevation and 8 km in distance. This small boundary region suggests that the balance between overburden-driven firn densification and melt-driven densification may be sensitive to small changes in melt. This could greatly influence changes in surface elevation of the GrIS in a changing climate.

## Appendix A

### A1. Inversion Setup and Rules

[35] In this appendix we describe our model setup and inversion rules. Here  $\nu$  is velocity; TWT is two-way traveltime; the subscripts  $t$  and  $b$  refer to the top and bottom of

a layer, respectively; and  $N$  refers to the layer number (i.e.,  $N = 3$  for the third layer).  $\text{TWT}_{\text{RMS}}$  is the RMS error of the fit between the ray trace model moveout curves and the picked moveout curves. The subscripts  $\text{NMO}$  and  $\text{DIX}$  are used to distinguish between velocities calculated from NMO measurements and velocities calculated using the Dix equation. We calculated stacking velocities for our starting models by linearly fitting the traveltime versus offset picks in the time-squared versus distance-squared domain; thus the stacking velocities are NMO approximations. We also calculated the standard deviation of the data to the NMO fit and used this value to determine whether our inversion was a “good” fit. For each horizon, we limited our fit to offsets in which the traveltime versus offset picks do not merge with the direct subsurface wave.

### A2. Linear Gradient Velocity Model Inversion

[36] We used six steps to form the linear gradient starting model:

[37] 1. The velocity at the surface ( $\nu 1_t$ ) is the direct subsurface wave velocity (Figure 3b).

[38] 2. Assume that  $\nu_{\text{NMO}}$  of the surface layer ( $\nu 1_{\text{NMO}}$ ) is the average velocity of that layer. The velocity at the base of that layer is then defined as  $\nu 1_b = 2\nu 1_{\text{NMO}} - \nu 1_t$  (Figure 5).

[39] 3. Set the velocity at the top of the second layer ( $\nu 2_t$ ) equal to  $\nu 1_b$ .

[40] 4. Let the Dix velocity of the second layer ( $\nu 2_{\text{DIX}}$ ) represent the average velocity of that layer. The velocity at the bottom of the second layer is then  $\nu 2_b = 2\nu 2_{\text{DIX}} - \nu 2_t$ .

[41] 5. Similarly, define all subsequent layers by setting  $\nu N_t = \nu(N-1)_b$  and  $\nu N_b = 2\nu N_{\text{DIX}} - \nu N_t$ , where  $N$  is the layer number.

[42] 6. Calculate the depth to each bulk layer boundary using the TWT for the near-offset trace and the  $\nu_{\text{NMO}}$  for the bulk layer(s).

[43] We used six steps in the linear gradient inversion:

[44] 1. Start with simplest (two-layer) model. The surface picked layer is the top bulk layer ( $N = 1$ ). All other picked layers are combined into one layer ( $N = 2$ ).

[45] 2. Invert for each bulk layer separately from top to bottom, starting with the second bulk layer.

[46] 3. Iteratively solve for depth and velocity of each bulk layer separately, keeping the top velocity equal to the velocity at the base of the previous bulk layer.

[47] 4. Iterate until the residual RMS traveltime between the modeled traveltime versus offset curve and the picked curves for all bulk layers is within 1 standard deviation of the NMO fit to bulk layers.

[48] 5. If the residual RMS traveltime between the modeled traveltime versus offset curve and the picked curves for all picked layers is within 2 standard deviations of the NMO fit to the picked layers, then no further changes in the model are justified and inversion is stopped.

[49] 6. If the fit to the picked layers is greater than 2 standard deviations of the NMO fit to the picked layers, then increase the number of bulk layers by one, holding the top bulk layer ( $N = 1$ ) constant, and redo inversion. For example, a model with three bulk layers would consist of the surface picked layer being the top bulk layer ( $N = 1$ ) and all other picked layers combined into two layers ( $N = 2$  and  $N = 3$ ). The location of the new layer boundary is where the modeled TWT curves deviate from the picked layers.

### A3. Stepped Velocity Model

[50] We used three steps to form the stepped velocity starting model:

[51] 1. Assume  $v_{\text{NMO}}$  of the surface layer ( $v_{1\text{NMO}}$ ) is the average velocity of that layer. Thus,  $v_1 = v_{1\text{NMO}}$ .

[52] 2. Assume the initial velocity for other bulk layers is  $v_{\text{DIX}}$  for those bulk layers (Figure 6).

[53] 3. Calculate the depth to each bulk layer boundary using the TWT for the near-offset trace and the  $v_{\text{NMO}}$  for the bulk layer(s).

[54] We used six steps in the stepped velocity inversion:

[55] 1. Start with simplest (two-layer) model in which the surface picked layer is the top bulk layer ( $N = 1$ ) and all other picked layers are combined into one layer ( $N = 2$ ).

[56] 2. Invert for each bulk layer separately from top to bottom, starting with the second bulk layer.

[57] 3. Solve for depth and velocity of each layer together.

[58] 4. Iterate until the residual RMS traveltime between the modeled traveltime versus offset curve and the picked curves for all bulk layers is within 1 standard deviation of the NMO fit to bulk layers.

[59] 5. If the residual RMS traveltime between the modeled traveltime versus offset curve and the picked curves for all picked layers is within 2 standard deviations of the NMO fit to the picked layers, then no further changes in the model are justified and inversion is stopped.

[60] 6. If the fit to the picked layers is greater than 2 standard deviations of the NMO fit to the picked layers, then increase the number of bulk layers by one, holding the top bulk layer ( $N = 1$ ) constant, and redo inversion. For example, a model with three bulk layers would consist of the surface picked layer being the top bulk layer ( $N = 1$ ) and all other picked layers combined into two layers ( $N = 2$  and  $N = 3$ ). The location of the new layer boundary is where the modeled TWT curves deviate from the picked layers.

[61] **Acknowledgments.** This work was funded by U.S. National Science Foundation grant OPP-ANS 0612506. We would like to thank Steve Arcone, Huw Horgan, and an anonymous reviewer for their insightful and thorough comments, which greatly improved this manuscript. We would also like to thank David Schuler and Daniel Sturgis for helping to collect radar data.

### References

- Abdalati, W. (2007), Greenland ice sheet melt characteristics derived from passive microwave data, 2 April 1979–31 October 2007, Natl. Snow and Ice Data Cent, Boulder, Colo., <http://nsidc.org/data/nsidc-0218.html>.
- Bales, R. C., Q. Guo, D. Shen, J. R. McConnell, G. Du, J. F. Burkhart, V. B. Spikes, E. Hanna, and J. Cappelen (2009), Annual accumulation for Greenland updated using ice core data developed during 2000–2006 and analysis of daily coastal meteorological data, *J. Geophys. Res.*, *114*, D06116, doi:10.1029/2008JD011208.
- Bamber, J. L., R. L. Layberry, and S. P. Gogenini (2001), A new ice thickness and bed data set for the Greenland ice sheet 1. Measurement, data reduction, and errors, *J. Geophys. Res.*, *106*(D24), 33,773–33,780, doi:10.1029/2001JD900054.
- Benson, C. S. (1960), Stratigraphic studies in the snow and firn of the Greenland ice sheet, Ph.D. diss., Calif. Inst. of Technol., Pasadena, Calif.
- Box, J. E., D. H. Bromwich, and L. S. Bai (2004), Greenland ice sheet surface mass balance 1991–2000: Application of Polar MM5 mesoscale model and in situ data, *J. Geophys. Res.*, *109*, D16105, doi:10.1029/2003JD004451.
- Bradford, J. H. (2002), Depth characterization of shallow aquifers with seismic reflection, Part I—The failure of NMO velocity analysis and quantitative error prediction, *Geophysics*, *67*, 89–97, doi:10.1190/1.1451362.
- Bradford, J. H., J. T. Harper, and J. Brown (2009), Complex dielectric permittivity measurements from ground-penetrating radar data to estimate snow liquid water content in the pendular regime, *Water Resour. Res.*, *45*, W08403, doi:10.1029/2008WR007341.
- Braithwaite, R. J., M. Laternser, and W. T. Pfeffer (1994), Variations of near-surface firn density in the lower accumulation area of the Greenland ice sheet, Pâkitsoq, West Greenland, *J. Glaciol.*, *40*(136), 477–485.
- Brown, J., J. Harper, W. T. Pfeffer, N. Humphrey, and J. Bradford (2011), High resolution study of layering within the percolation and soaked facies of the Greenland ice sheet, *Ann. Glaciol.*, *52*(59), 35–42.
- Dix, C. H. (1955), Seismic velocities from surface measurements, *Geophysics*, *20*, 68–86, doi:10.1190/1.1438126.
- Dunse, T., O. Eisen, V. Helm, W. Rack, D. Steinhage, and V. Parry (2008), Characteristics and small-scale variability of GPR signals and their relation to snow accumulation in Greenland's percolation zone, *J. Glaciol.*, *54*(185), 333–342, doi:10.3189/002214308784886207.
- Fausto, R., A. Ahlstrom, D. Van As, C. Boggild, and S. Johnsen (2009), A new present-day temperature parameterization for Greenland, *J. Glaciol.*, *55*(189), 95–105, doi:10.3189/002214309788608985.
- Fischer, H., D. Wagenbach, M. Laternser, and W. Haeberli (1995), Glacio-meteorological and isotopic studies along the EGIG line, central Greenland, *J. Glaciol.*, *41*(139), 515–527.
- Hanna, E., P. Huybrechts, I. Janssens, J. Cappelen, K. Steffen, and A. Stephens (2005), Runoff and mass balance of the Greenland ice sheet: 1958–2003, *J. Geophys. Res.*, *110*, D13108, doi:10.1029/2004JD005641.
- Harper, J. T., and J. H. Bradford (2003), Snow stratigraphy over a uniform depositional surface: Spatial variability and measurement tools, *Cold Reg. Sci. Technol.*, *37*, 289–298, doi:10.1016/S0165-232X(03)00071-5.
- Helsen, M. M., M. R. van den Broeke, R. S. W. van de Wal, W. J. van de Berg, E. van Meijgaard, C. H. Davis, Y. Li, and I. Goodwin (2008), Elevation changes in Antarctica mainly determined by accumulation variability, *Science*, *320*, 1626–1629, doi:10.1126/science.1153894.
- Hempel, L., F. Thyssen, N. Gundestrup, H. B. Clausen, and H. Miller (2000), A comparison of radio echo sounding data and electrical conductivity of the GRIP ice core, *J. Glaciol.*, *46*(154), 369–374, doi:10.3189/172756500781833070.
- Herron, M. M., and C. C. Langway Jr. (1980), Firn densification: An empirical model, *J. Glaciol.*, *25*(93), 373–385.
- Holland, P. R., H. F. J. Corr, H. D. Pritchard, D. G. Vaughan, R. J. Arthern, A. Jenkins, and M. Tedesco (2011), The air content of the Larson Ice Shelf, *Geophys. Res. Lett.*, *38*, L10503, doi:10.1029/2011GL047245.
- Hörhold, M. W., S. Kipfstuhl, F. Wilhelms, J. Freitag, and A. Frenzel (2011), The densification of layered polar firn, *J. Geophys. Res.*, *116*, F01001, doi:10.1029/2009JF001630.
- Hou, S., and D. Qin (2002), The effect of postdepositional process on the chemical profiles of snow pits in the percolation zone, *Cold Reg. Sci. Technol.*, *34*(2), 111–116, doi:10.1016/S0165-232X(01)00065-9.
- Knight, R., P. Tercier, and J. Irving (2004), The effect of vertical measurement resolution on the correlation structure of a ground penetrating radar reflection image, *Geophys. Res. Lett.*, *31*, L21607, doi:10.1029/2004GL021112.
- Legarsky, J. J., and X. Gao (2006), Internal layer tracing and age-depth relationship from the ice divide toward Jacobshavn, Greenland, *IEEE Geosci. Remote Sens. Lett.*, *3*(4), 471–475, doi:10.1109/LGRS.2006.877749.
- Maeno, N., and T. Ebinuma (1983), Pressure sintering of ice and its implication to the densification of snow at polar glaciers and ice sheets, *J. Phys. Chem.*, *87*(21), 4103–4110, doi:10.1021/j100244a023.

- McConnell, J. R., R. J. Arthern, E. Mosley-Thompson, C. H. Davis, R. C. Bales, R. Thomas, J. F. Burkhart, and J. D. Kyne (2000), Changes in Greenland ice sheet elevation attributed primarily to snow accumulation variability, *Nature*, *406*, 877–879, doi:10.1038/35022555.
- Mosley-Thompson, E., J. R. McConnell, R. C. Bales, Z. Li, P.-N. Lin, K. Steffen, L. G. Thompson, R. Edwards, and D. Bathke (2001), Local to regional-scale variability of Greenland accumulation from PARCA cores, *J. Geophys. Res.*, *106*(D24), 33,839–33,851, doi:10.1029/2001JD900067.
- Murray, T., A. Booth, and D. M. Rippin (2007), Water-content of glacier-ice: Limitations on estimates from velocity analysis of surface ground-penetrating radar surveys, *J. Environ. Eng. Geophys.*, *12*(1), 87–99, doi:10.2113/JEEG12.1.87.
- Nghiem, S. V., K. Steffen, G. Neumann, and R. Huff (2005), Mapping of ice layer extent and snow accumulation in the percolation zone of the Greenland ice sheet, *J. Geophys. Res.*, *110*, F02017, doi:10.1029/2004JF000234.
- Parry, V., P. Nienow, D. Mair, J. Scott, B. Hubbard, K. Steffen, and D. Wingham (2007), Investigations of meltwater refreezing and density variations in the snowpack and firn within the percolation zone of the Greenland ice sheet, *Ann. Glaciol.*, *46*(1), 61–68, doi:10.3189/172756407782871332.
- Paterson, W. S. B. (1994), *The Physics of Glaciers*, 3rd ed., Pergamon, Oxford, U. K.
- Pfeffer, W. T., M. F. Meier, and T. H. Illangasekare (1991), Retention of Greenland runoff by refreezing: Implications for projected future sea level change, *J. Geophys. Res.*, *96*(C12), 22,117–22,124, doi:10.1029/91JC02502.
- Steffen, K., J. E. Box, and W. Abdalati (1996), Greenland Climate Network: GC-Net, in *Special Report on Glaciers, Ice Sheets and Volcanoes: A Tribute to Mark F. Meier*, edited by S. C. Colbeck et al., pp. 98–103, U.S. Army Cold Regions Res. and Eng. Lab., Hanover, N. H.
- Tiuri, M. E., A. Sihvola, E. Nyfors, and M. Hallikaiken (1984), The complex dielectric constant of snow at microwave frequencies, *IEEE J. Oceanic Eng.*, *9*(5), 377–382, doi:10.1109/JOE.1984.1145645.
- Wharton, R. P., R. N. Rau, and D. L. Best (1980), Electromagnetic propagation logging: Advances in technique and interpretation, paper presented at the SPE Annual Technical Conference and Exhibition, Soc. of Pet. Eng., Dallas, Tex., 21–24 September, doi:10.2118/9267-MS.
- Yilmaz, Ö. (2001), *Seismic Data Analysis: Processing, Inversion, and Interpretation of Seismic Data*, Soc. of Explor. Geophys., Tulsa, Okla., doi:10.1190/1.9781560801580.
- Zelt, C. A., and R. B. Smith (1992), Seismic traveltime inversion for 2-D crustal velocity structure, *Geophys. J. Int.*, *108*(1), 16–34, doi:10.1111/j.1365-246X.1992.tb00836.x.
- Zwally, H. J., and J. Li (2002), Seasonal and interannual variations of firn densification and ice-sheet surface elevation at the Greenland summit, *J. Glaciol.*, *48*(161), 199–207, doi:10.3189/172756502781831403.
- Zwally, H. J., M. B. Giovinetto, J. Li, H. G. Cornejo, M. A. Beckley, A. C. Brenner, J. L. Saba, and D. Yi (2005), Mass changes of the Greenland and Antarctic ice sheets and shelves and contributions to sea level rise: 1992–2002, *J. Glaciol.*, *51*(175), 509–527, doi:10.3189/172756505781829007.

---

J. Bradford and J. Brown, Center for Geophysical Investigation of the Shallow Subsurface, Boise State University, 1910 University Dr., Boise, ID 83725, USA. (jbrown@cgiss.boisestate.edu)

J. Harper, Geosciences Department, University of Montana, 32 Campus Drive #1296, Missoula, MT 59812-1296, USA.

N. Humphrey, Department of Geology and Geophysics, University of Wyoming, 1000 University Ave., Laramie, WY 82071-3006, USA.

E. Mosley-Thompson, Byrd Polar Research Center, Room 108, Scott Hall, 1090 Carmack Rd., The Ohio State University, Columbus, OH 43210, USA.

W. T. Pfeffer, Institute of Arctic and Alpine Research, Campus Box 450, University of Colorado Boulder, Boulder, CO 80301, USA.